Supporting Information for

Mid-Infrared Time-Resolved Frequency Comb Spectroscopy of Transient Free Radicals

Adam J. Fleisher[*,†,‡], *Bryce J. Bjork*[†], *Thinh Q. Bui*[§], *Kevin C. Cossel*[†], *Mitchio Okumura*[§], *Jun Ye*[*,†]

[†]JILA, National Institute of Standards and Technology and University of Colorado, Department of Physics, Boulder, CO 80309, USA.

[‡]Material Measurement Laboratory, National Institute of Standards and Technology, Gaithersburg, MD 20899, USA.

[§]Arthur Amos Noyes Laboratory of Chemical Physics, Division of Chemistry and Chemical Engineering, California Institute of Technology, Pasadena, CA 91125, USA.

AUTHOR INFORMATION

Corresponding Authors

*adam.fleisher@nist.gov, ye@jila.colorado.edu

Supporting Materials and Methods:

The photolysis experiments described here were conducted in a flow cell coupled to a high-finesse optical cavity similar to that described in the Supplementary Material for Ref. 28 of the main text and illustrated in Fig. S1. The gas flow rates of three different inlets (two purge, one sample) were set such that the pressure in the photolysis region of the cavity was maintained at 1.60 kPa ± 0.02 kPa. The N_2 purge inlets located near each high-reflectivity mirror were set at a total flow of 400 sccm (200 sccm through each) as controlled by a fine needle valve.

Mono-deuterated acrylic acid, AA-d_1, was synthesized by mixing D_2O with commercial acrylic acid (Sigma Aldrich, 99% purity) for several hours; the sample was extracted with methylene chloride and purified by roto-evaporation as outlined by Petty and Moore in Ref. 26 of the main text. Care was taken to exclude water (H_2O) from the liquid AA-d_1 precursor during synthesis. The AA-d_1 sample was confirmed by both proton and deuterium NMR to have been synthesized with 90% isotopic efficiency, and no resonances originating from water were observed. We found a very small amount of hydrocarbon contamination at low NMR shifts (~0.85 and 1.3 ppm in $CDCL_3$). These resonances, not present in the commercial undeuterated AA sample, can be attributed to a small amount of vacuum grease.

The same research grade N_2 was supplied to a temperature-controlled bubbler (20.00 °C ± 0.07 °C) containing AA-d_1 at a rate of 10 sccm. Bubbling was slowed to a rate of tens of fine bubbles per second using a valve located between the AA-d_1 liquid bubbler and the flow cell while maintaining constant flow rates. Just before expansion into the flow cell, the N_2/AA-d_1 sample was mixed in a stainless steel tee of diameter 0.635 cm with 80 sccm of research grade CO_2 in order to increase vibrational cooling of hot DOCO formed during photolysis. For the current experiments, to minimize contamination of the high reflectivity mirrors, we used purge flows

(400 sccm) that were substantially higher than the flow of reagent and carrier gas introduced through the central inlet (90 sccm). This arrangement led to further dilution of the AA-d_1 and may have resulted in a gradient along the probe axis, with AA-d_1 concentration highest in the center of the cell, by the inlet.

The ArF excimer that initiated acrylic acid-d_1 (AA-d_1) photolysis was operated at an output power of 10 mJ/pulse and a repetition rate of 0.2 Hz. The beam was steered using two highly-reflective mirrors coated for 193 nm. Together, these two mirrors had a reflection coefficient of 77%. The photolysis laser window through which the 193 nm pulse entered the high-finesse cavity flow cell was an uncoated UV fused silica plate ≈1 mm thick, with a measured transmission coefficient of 62%. Consequently, only 4.8 mJ per photolysis pulse reached the molecules within the flow cell. The entire photolysis beam cross-sectional area was 3 cm × 1 cm at the photolysis laser window, with the 3 cm width aligned parallel to the mid-infrared (mid-IR) optical axis. The vertical beam profile possessed a roughly Gaussian shape with a full width at half maximum of 5.4 mm ± 0.2 mm measured with a knife edge and power meter. The photolysis windows were carefully cleaned and dried under vacuum for several hours before a series of single-photolysis-pulse experiments were performed. An illustration of the flow cell coupled to a high finesse optical cavity is shown in Fig. S1.

The mid-IR frequency comb was operated with an average power of 500 mW before entering the high-finesse cavity, and had a full width at half maximum (FWHM) bandwidth of 150 cm^{-1}. For detection of *trans*-DOCO, HOD, D_2O, and AA-d_1, the center wavelength was 3.73 μm. The comb repetition rate (f_{rep}) was 136.5 MHz, which is equal to one-half the high-finesse cavity free spectral range (FSR). This condition, where $2f_{rep}$ = FSR, results in half the mid-IR frequency comb teeth being rejected by the optical cavity, and the comb mode spacing observed by the

VIPA spectrometer is 273 MHz, well below its measured resolving power at a 15° tilt angle of 1.0 GHz ± 0.1 GHz. Over the 64.4 cm^{-1} simultaneous bandwidth recorded by the VIPA spectrometer, 7072 frequency comb teeth are incident on the VIPA following transmission through the high-finesse cavity. The VIPA resolution therefore limits the number of resolvable spectral elements to 1930. All elements spanning the 64.4 cm^{-1} bandwidth are recorded in as little as 25 μs.

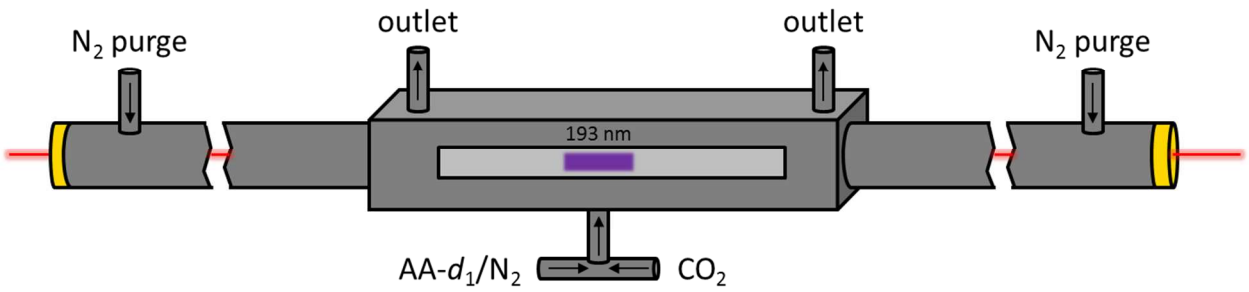

Fig. S1. Mass flow cell coupled to a high-finesse optical cavity (length not drawn to scale, as indicated by the breaks in each cylindrical purge arm). Arrows on the inlet/outlet ports indicate the direction of mass flow. The distance between the two highly-reflective low-loss optics (gold color above) is the optical cavity length, L_{cav} = 54.88 cm. The photolysis pathlength, L_{phot}, is equivalent to the width of the 193 nm excimer pulse (purple, traveling in and out of the page) shown irradiating the photolysis laser window (light gray). The mid-infrared frequency comb is shown in red, traveling perpendicular to the photolysis pulse.

The C_2HD spectrum was observed in a separate spectral window, centered at 3.93 μm (2545 cm^{-1}). In order to record time-resolved spectra from a different portion of the cavity-transmitted mid-IR frequency comb, we simply tuned the ruled diffraction grating located at the output of the

tilted VIPA etalon. More details on the entire 2-D dispersive spectrometer are available in Ref. 29 of the main text (and references therein).

Supporting Text:

Fitting Procedure: In direct absorption spectroscopy, the measured absorption coefficient $\alpha(\tilde{\nu})$ is related to the absolute concentration of the absorbing species via (ES1),

$$\alpha(\tilde{\nu}) = SNg(\tilde{\nu} - \tilde{\nu}_0) \quad \text{(ES1)}$$

where S is the molecular line strength in cm per molecule, N is the molecular density of absorbers in cm^{-3} (normalized to 101.325 kPa), and $g(\tilde{\nu} - \tilde{\nu}_0)$ is the normalized lineshape function in cm.

The molecular line strengths S for HOD mid-IR transitions are available in the HITRAN database (*S1*). The line strengths for D_2O infrared transitions were measured by Robert A. Toth at Caltech/JPL, and generously provided through private communication with Keeyoon Sung of JPL (line positions available in Ref. *S2*). Line strengths for the ν_1 band of *trans*-DOCO, however, have not been reported. In order to generate a line list for the ν_1 band at 2684 cm^{-1}, the previously measured rotational parameters in the ground and excited vibrational states from Ref. 26 of the main text were used in combination with a calculated total band intensity available in Ref. 32 of the main text and simulated in PGOPHER at a rotational temperature of 295 K (*S3*).

Each molecular line list containing center frequencies and line strengths were broadened using a single Gaussian normalized lineshape function $g(\tilde{\nu} - \tilde{\nu}_0)$, with a fixed FWHM of 1.0 GHz. The VIPA spectrometer-limited FWHM was measured independently using known methane (CH_4) infrared lines and confirmed by the presence of low residuals following the subtraction of

molecular fits. Since these CH_4 lines were not measured contemporaneously in the current experiment, there is some minor discrepancy between certain simulated widths and fitted peak heights. Since we employ a global fit of all peaks within our spectral bandwidth, the uncertainty in the absolute frequency axis (<1 GHz) is directly related to our uncertainty in the integrated area of all peaks belonging to a single molecular species, and therefore makes an implicit contribution to our reported molecular sensitivities.

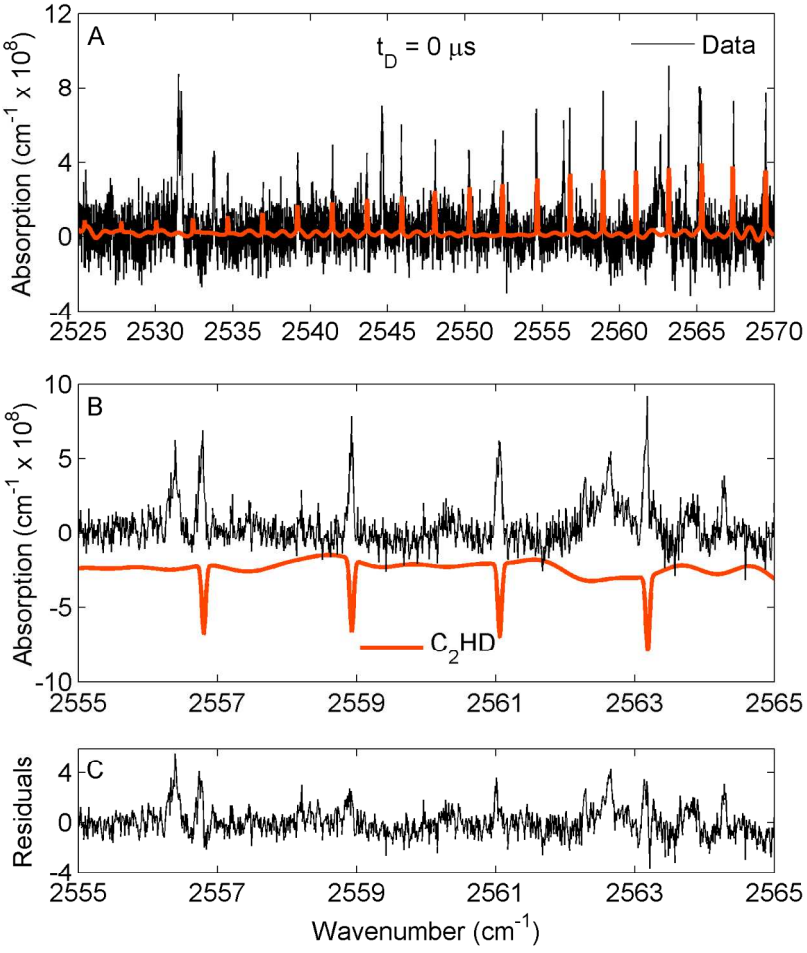

Fig. S2. Absorption spectrum of C_2HD at a time delay of t_D = 0 μs following 193 nm laser photolysis of acrylic acid-d_1. (**A**) The data (black) is the result of 1000 averages at an individual camera integration time of 50 μs. The fit C_2HD absorption spectrum is shown superimposed in orange on the black experimental data. (**B**) A zoom of the experimental data show in (**A**) with the

fit C_2HD spectrum (orange) inverted and offset (by 2×10^{-8} cm^{-1}) for clarity. A 5th order polynomial baseline function and the intensities of about ten periodic baseline oscillations were also included in the fit. (**C**) Fit residuals. Absorption features in (**A-C**) not assigned to C_2HD are only present at t_D = 0 μs, whereas C_2HD persists until the flow cell is refreshed (see Fig. S6).

We determined the absolute time-dependent concentrations of HOD, D_2O, and *trans*-DOCO by fitting their experimental spectra (in units of $\alpha(\tilde{\nu})$), recorded at varying time delays following photolysis. We fit intensities of all lines of each molecular spectrum simultaneously to a broadened model line spectrum, along with a 5th order polynomial baseline function and the amplitudes of about ten periodic baseline functions (both *sine* and *cosine* components) of fixed frequencies extracted from a Fourier transform of the one-dimensional absorption spectra. In Figs. 2-3 of the main text, the baseline polynomial, periodic oscillations, and the AA-d_1 photo-depletion spectrum have been subtracted from the experimental traces, leaving only the molecular contributions and high-frequency noise.

A majority of the C_2HD ν_3 *P*-branch can be seen in Fig. S2, with the TRFCS spectral window centered at 2545 cm^{-1} (near the calculated ν_1 band center of *cis*-DOCO reported in Ref. 32 of the main text). For spectral fitting, a C_2HD line list was generated in PGOHPER (*S3*) at a rotational temperature of 295 K using previously measured rotational parameters from Ref. *S4* and a calculated fundamental band intensity of 20.6 km/mol. In order to obtain the unknown band intensity, the optimized geometry and fundamental vibrational frequencies and intensities (including anharmonic corrections calculated using second order vibrational perturbation theory VPT2) of C_2HD were calculated at the CCSD(T)/aug-pVDZ level using the CFOUR program (*S5*).

Total Experimental Uncertainty: For the linear fitting of molecular spectra described above, a theoretical spectrum of concentration C was simulated for each species and fit to a linear scaling factor N. The fit concentration NC was then converted from units of μmol/mol to molecular concentration units (cm^{-3}) using the Loschmidt constant (N_L) at experimental pressure and temperature. In addition, the difference in total optical cavity length (L_{cav}) and photolysis pathlength (L_{phot}) was taken into account when reporting photoproduct concentrations. The final expression for photoproduct molecular concentration in cm^{-3} is shown below.

$$C_f = NCN_L \frac{L_{cav}}{L_{phot}} \tag{ES2}$$

Each quantity in Eq. ES2 has an associated experimental uncertainty. The uncertainty in N is extracted as described in Ref. 27 of the main text using known multiline fitting procedures. For the band intensity of *trans*-DOCO, we estimate the uncertainty in C to be $\sigma_C = 0.1 \times C$ (10% uncertainty), which we postulate entirely from the calculated intensity reported by Huang *et al.* (Ref. 32 of the main text). The uncertainty in N_L is related to the uncertainty in our measurement of intracavity pressure, which was done using a pressure gauge with an observed precision of 1% ($\sigma_{NL} = 0.01 \times N_L$). The optical cavity length is known to much higher precision, and was monitored continuously by recording the eight harmonic of the repetition rate of the mode-locked OPO pump laser during the experiment. Its uncertainty is not considered to play a significant role compared to other sources. The photolysis pathlength, however, has an estimated uncertainty of 0.3 cm, or 10% of the measured excimer beam width at the flow cell. Finally, the experimental uncertainty in C_f is calculated using Eq. ES3 below.

$$\sigma_{C_f}^2 = \left(\frac{\partial C_f}{\partial N}\right)^2 \sigma_N^2 + \left(\frac{\partial C_f}{\partial C}\right)^2 \sigma_C^2 + \left(\frac{\partial C_f}{\partial N_L}\right)^2 \sigma_{N_L}^2 + \left(\frac{\partial C_f}{\partial L_{phot}}\right)^2 \sigma_{L_{phot}}^2 \tag{ES3}$$

There may be gradients in concentrations along the probe beam axis, due to the flow conditions. While we measure the column densities accurately, our computed concentrations should be considered an average value over the appropriate effective cavity length (L_{phot}, L_{cav}, etc). The gradient, however, should not otherwise affect the results reported here, since we are not measuring bimolecular rate constants in the current experiment. The potential for unwanted gradients will be greatly reduced in future experiments by decreasing the purge flow to a value commensurate with the sample inlet flow.

For *trans*-DOCO, the following parameters were used to determine C_f and σ_{Cf}: $N = 0.43$, $C = 1.0$ μmol/mol, $N_L = 3.94\times10^{17}$ cm^{-3}, $L_{cav} = 54.88$ cm, $L_{phot} = 3.0$ cm, $\sigma_N = 0.02$, $\sigma_C = 0.1$ μmol/mol, $\sigma_{NL} = 4 \times 10^{15}$ cm^{-3}, and $\sigma_{Lphot} = 0.3$ cm. Therefore, we report in the main text, as measured in a typical run, a *trans*-DOCO molecular concentration of $C_f = 3.1\times10^{12}$ cm^{-3} ± 0.5×10^{12} cm^{-3} for $t_D = 0$ μs with an integration time of 50 μs and 950 averages. It is worth noting that the contribution to σ_{Cf} that arises solely from spectral fitting and observed signal-to-noise (σ_N) is an order of magnitude better than the overall experimental uncertainty reported here. Thus, we report a *trans*-DOCO sensitivity of 5×10^{10} cm^{-3}.

Time-Resolved Frequency Comb Spectroscopy Performance: The figure-of-merit used in comparison with other direct absorption techniques is the noise-equivalent absorption (NEA) normalized to 1 s of averaging time. In time-resolved frequency comb spectroscopy (TRFCS) we have the unique ability to recorded hundreds of broadband absorption spectra in rapid succession. An illustration of our data acquisition scheme is shown in Fig. S3.

For comparison with continuous-wave (cw) absorption techniques we calculate a bandwidth normalized NEA, known as NEA per spectral element, since many spectral elements are resolved simultaneously in a single TRFCS experiment. This can be expressed as

$$NEA = \sigma_{noise} \frac{\pi}{FL_{phot}} \sqrt{\frac{T}{M}} \qquad \text{(ES4)}$$

where σ_{noise} is the standard deviation of the noise in absorbance (absorbance $A = 1 - I/I_0$, where I is the light acquired in each VIPA image in the presence of photolysis products and I_0 is the reference light acquired in VIPA images recorder prior to photolysis), F is the measured cavity finesse, L_{phot} is the optical pathlength over which photolysis can occur, T is the total camera integration time required to record two images (one reference and one signal), and M is the number of resolvable spectral elements per image. A representative set of experimental conditions are as follows: $\sigma_{noise} = 6\times10^{-3}$, F = 1250 at 2684 cm^{-1}, L_{phot} = 3 cm, $T = 2\times50$ μs = 100 μs, and M = 1930 elements. Therefore, in this initial demonstration of mid-IR TRFCS, we measure NEA = 1.1×10^{-9} cm^{-1} $Hz^{-1/2}$ per spectral element.

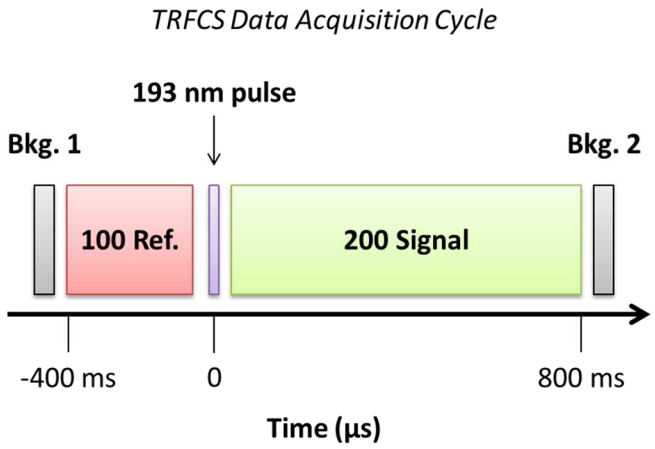

Fig. S3. Illustration of TRFCS data acquisition scheme. The time axis and blocks are not drawn to scale. The individual VIPA images that comprise the reference (abbreviated Ref. above) and signal blocks above were acquired at a camera-limited frame rate of 250 Hz. The 100 reference images are averaged and used as a single reference for the 200 time-resolved signal images recorded following photolysis. The integration time for each individual image was either 25 μs

(camera-limited) or 50 μs. Camera background images recorded with the mid-infrared frequency comb blocked (Bkg. 1 and 2) were taken before and after a single TRFCS cycle in order to subtract camera dark counts.

We use the above observed absorption noise, measured finesse, and cavity length to estimate our OD sensitivity within this spectral region of the mid-IR. Looking at the line list reported in Abrams *et al*. (*S6*), the *R*1(1.5) lines of the 1←0 vibrational band of OD should appear at 2676.7 cm^{-1}, near the center of the broadband spectral window shown in Fig. 2 of the main text. We estimate the line strength of these transitions to be equal to the line strength of the same *R*1(1.5) transitions in OH, but scaled by the ratio of the OD fundamental vibration band origin to that of OH. Therefore, $S_{OD} \approx 3.5\times10^{-20}$ cm/molecule. Taking the maximum of a Gaussian lineshape function of 1 GHz FWHM, we calculate our single-line minimum detectable concentration for OD to be 5×10^{12} cm^{-3} (without averaging).

Osborne, Li, and Smith have reported in Ref. 37 of the main text nearly equivalent AA photolysis yields for HOCO, CO_2, and CO under similar experimental conditions. Assuming all photolysis reactions that lead to CO formation also promptly form OH as an upper bound, we can estimate an upper-bound for the expected formation of OD in our experiment to be [OD] = [*trans*-DOCO] = 3×10^{12} cm^{-3}. Therefore, we do not expect significant absorption features from OD in our current TRFCS experiments. On the μs timescale, when both *trans*-DOCO and HOD are also present, spectroscopic interferences could also limit our realistic ability to spectroscopically identify OD, since only a handful of OD features exist even within our broad spectral window.

Initial AA-d_1 Concentration and Gas Residence Time: We could directly observe AA-d_1 by its fundamental ν_1 band (OD stretch) absorption spectrum. An absorption spectrum of the precursor

mixture N_2/CO_2/AA-d_1 recorded under typical flow conditions is shown in Fig. S4. The observed spectrum (blue) matches well with the OH-stretch absorption band of undeuterated acrylic acid recorded at a temperature of 50 °C and a pressure of 101.325 kPa (1 atmosphere) from Ref. *S7*, shown in red. The red trace is obtained by shifting the origin of the known undeuterated AA spectrum (PNNL database) and scaling the overall intensity to match the observed band. The origin frequency (and overall intensity) was scaled by a factor of approximately $\approx 1/\sqrt{2}$, consistent with deuteration. We observe additional structure in the AA-d_1 OD-stretch absorption spectrum due to the presence of periodic baseline functions.

We could use the known cross sections of the undeuterated OH-stretch spectrum to estimate the concentration of AA-d_1 monomers. We can correct for the effect of deuteration using a density functional theory calculation (*S8,S9*) at the B3LYP/6-311++G level, which suggests that the integrated intensity of the OD-stretch of AA-d_1 is approximately 20% lower than that of the OH stretch intensity in AA. From the spectrum shown in Fig. S4, recorded under typical flow conditions, we estimate a partial pressure of AA-d_1 monomers to be on the order of 10^{14} cm^{-3} ($p_{AA} \approx 2$ Pa). This value is roughly consistent with calculations based on the flow conditions, though we find that the latter consistently underestimates the AA-d_1 concentration, most likely due to unsaturated bubbler conditions and inhomogeneous mixing within the outlet-to-outlet region of the flow cell of the low flow of precursor mixture from the inlet with the much higher purge flow of N_2. Given the uncertainties in flow conditions, the spectrum thus provides a more direct and reliable estimate of AA-d_1 concentrations. We found that AA-d_1 concentrations varied with flow settings, most likely due to incomplete saturation in the bubbler and to limitations of the current flow meters. Since our primary goal of the current experiment was to detect DOCO

radicals and determine the sensitivity of the TRFCS technique, we did not record AA-d_1 spectra prior to every run and hence cannot report absolute quantum yields.

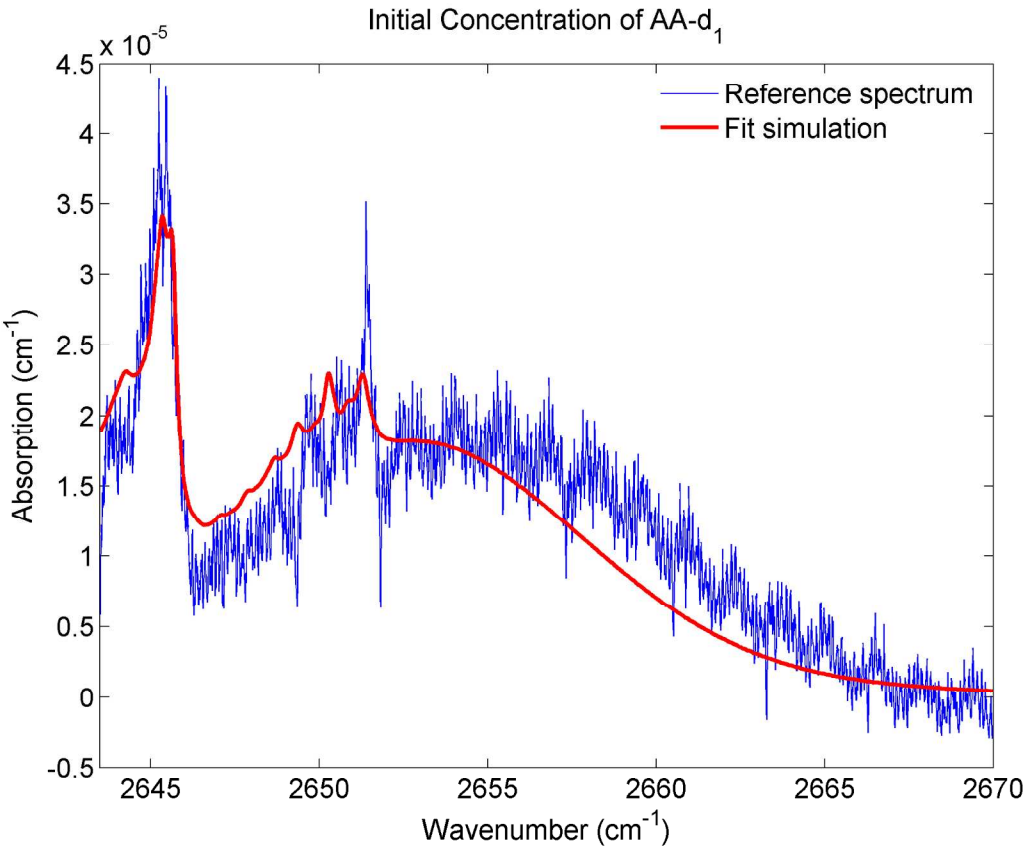

Fig. S4. Typical broadband absorption spectrum of acrylic acid-d_1 (AA-d_1) in blue, averaging 950 spectra. A shifted spectrum of undeuterated acrylic acid (AA) taken from the PNNL database (*S7*) is shown in red. Fine structure that appears in the blue trace is due to periodic baseline oscillations and not highly resolved ro-vibrational features of the AA-d_1 band. The average initial AA-d_1 molecular concentration is estimated above from the shifted and scaled AA band intensity to be $\approx 4\times10^{14}$ cm^{-3} over the entire 12 cm central region of the flow cell (outlet-to-outlet, see Fig. S1), assuming even mixing within this high-flow region.

In Fig. S5, we show the recovery of the AA-d_1 depletion as the gas in the photolyzed volume in pumped away and refreshed. At each delay time t_D, the spectrum (a representative spectrum is

shown as the blue trace shown in Fig. S4) was smoothed using a low pas filter function and integrated to determine the percent depletion of AA-d_1 following photolysis. After a single 193 nm pulse (time zero), the initial AA-d_1 concentration is depleted by ≈1.6% (extrapolated to a delay of t_D = 0 ms) relative to the typical initial spectrum shown in Fig. S4. The blue curve in Fig. S5 is a fit to an exponential decay, with an amplitude of 1.61% ± 0.04% and a decay coefficient k_{pump} = 3.0 s^{-1} ± 0.1 s^{-1} (1σ statistical uncertainty from the fit). This value agrees well with the decay constant at long times of ≈3 s^{-1} of the HOD concentration.

The photodepletion of AA-d_1 at t_D = 0 μs provides the AA-d_1 absorption cross section σ_{AA}

$$\frac{[AA]}{[AA]_0} = 1 - \exp(-\sigma_{AA}\Phi H), \qquad \text{(ES5)}$$

where Φ is the photodissociation quantum yield and H is the laser fluence divided by the photon energy (photon cm^{-2}). Assuming Φ = 1 and a laser fluence calculated from the excimer parameters, we estimate $\sigma_{AA} = 1\times10^{-17}$ cm^2 at 193 nm, in good agreement with that reported in Fig. 1 of Ref. *S10* and noted in Ref. 34 of the main text.

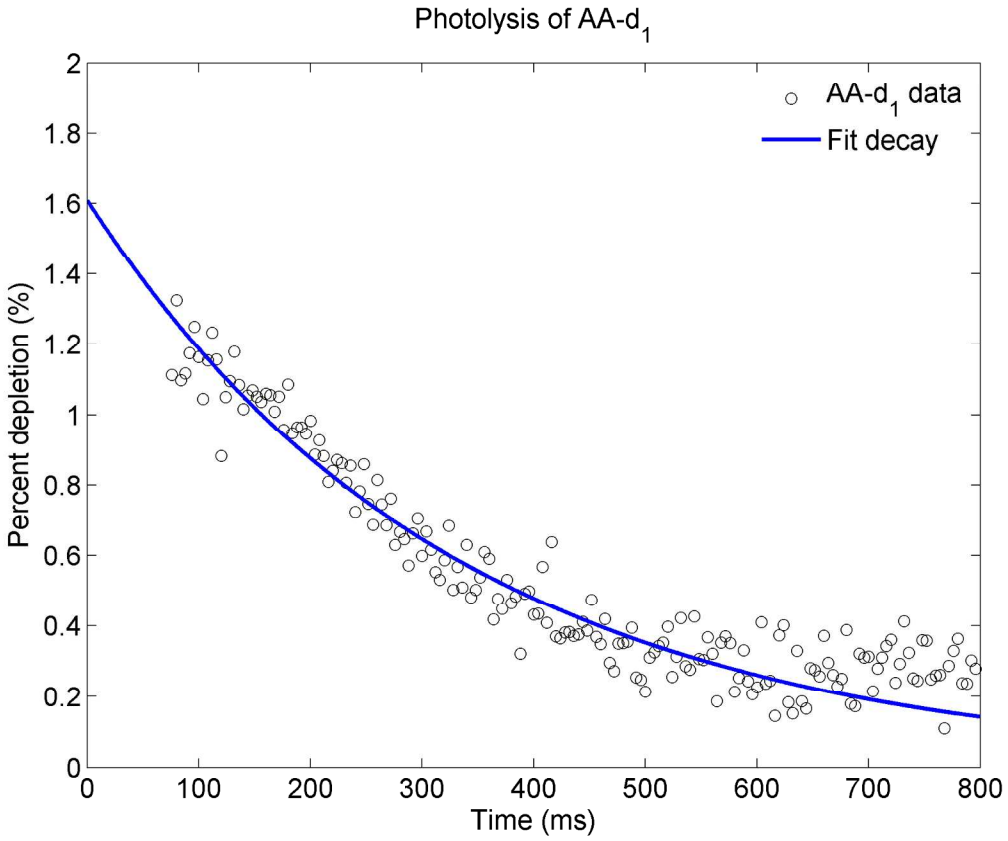

Fig. S5. Percent depletion of the integrated AA-d_1 band intensity as a function of time after the 193 nm photolysis pulse. Each data point in Fig. S5 is an average of 950 duty cycles at an integration time of 50 μs. The fit decay curve is a measure of the gas residence time within the high-finesse cavity flow cell. The fit decay constant is $k_{pump} = 3.0 \pm 0.1\ s^{-1}$.

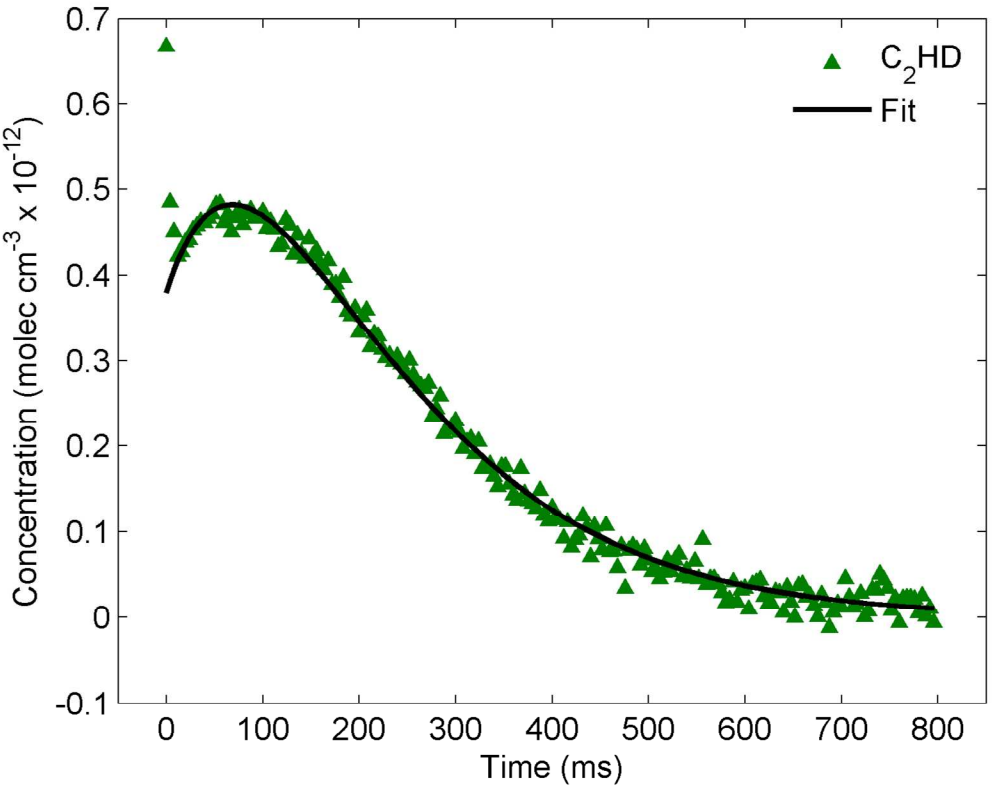

Fig. S6. Unobscured plot of the measured C_2HD concentration versus time following the photolysis of AA-d_1. Note that C_2HD is formed immediately ($t_D = 0$), therefore making it a direct product of AA-d_1 photodissociation. The biexponential fit (black) excludes data measured at times $t_D \leq 12$ ms (the first three data points).

Time-dependent Acetylene-d_1 concentration: The measured time-dependent absolute concentration of C_2HD is plotted in Fig. S6, as well as in Fig. 4 of the main text. The initial molecular concentration of C_2HD in the 50 μs immediately following photolysis was 7×10^{11} cm^{-3} with an experimental uncertainty of $\pm3\times10^{11}$ cm^{-3}. We observe an initial decay of C_2HD of approximately 30% in the first 4 ms. Since, following initial formation, C_2HD does not undergo subsequent reactions, we attribute this decay to fast local diffusion of primary photoproducts out of the probe volume (1.2 mm cavity waist at the center of the flow cell). This arises from both

the non-uniform illumination of the sample by the excimer beam and any inhomogeneous distribution of reagent AA-d_1 within the flow cell caused by the high purge flows. Diffusion must also be partially responsible for a small fraction of the initial 4 ms decay of HOD (panels A and B of Fig. 4 of the main text), but isotope exchange reactions must contribute to most of the decay, especially after 4 ms. The magnitude of HOD loss due to exchange reactions can be seen in the concomitant rise of D_2O products (panels A and B, Fig. 4), which is not formed as a primary photoproduct. Again, roughly 30% of the HOD loss, occurring in the first 4 ms, cannot be accounted for by reaction and is consistent with early diffusional loss. The *trans*-DOCO reacts too rapidly to be affected by diffusion. As was the case for HOD and D_2O, the C_2HD concentration at $t_D > 100$ ms is dominated by the gas residence time within the flow cell.

***Short Time Diffusional Loss*:** The transient decays in C_2HD and HOD products in the first few milliseconds arise from diffusion out of the prove volume, in the direction transverse to the cavity optical axis. Along this direction, the excimer laser responsible for photolysis is only about a factor of 5 larger in beam waist than the cavity probe beam. The photolysis volume has a cross-sectional area of 3 cm × 1 cm, whereas the probe volume is defined by the cavity waist radius of ≈1.2 mm. While the photolysis volume is much larger than the probe, the excimer laser power is not evenly distributed throughout the photolysis volume. We have made knife edge measurements of the vertical (1 cm) excimer beam profile which indicate a roughly Gaussian power distribution, whereas the horizontal (3 cm) beam profile appears to have a more complicated shape. As the measured absorption is integrated over the horizontal beam profile, diffusion in this dimension should play a smaller role than diffusion in the vertical. We have modeled the diffusion as a one-dimensional problem involving a Gaussian distribution of photoproducts with a FWHM = 0.54 cm. Under our experimental conditions (T = 21 °C, P =1.6

kPa, average molecular diameter of $d \approx 300$ pm), we calculate the diffusion coefficient of C_2HD in N_2 to be $D_{C2HD} = 20$ cm^2 s^{-1}. We find that the modeled decay is in good agreement with the initial decay observed for C_2HD. We obtain similar results for HOD.

***Possible Sources of Photoproducts HOD and C_2HD*:** We observe HOD and C_2HD products that are formed, within the first 25-50 μs, prior to any secondary chemistry. We hypothesize that these are formed from the unimolecular photodissociation of acrylic acid, but we acknowledge that we cannot yet exclude all other explanations without further experiments. Among the possible alternatives, we consider below issues related to cluster formation, H_2O contamination and wall effects.

Acrylic acid is well known to form dimers or larger clusters at room temperature. The new photoproducts could in principle arise from the photolysis of clusters. However, we estimate the fraction of dimers to be <1%, based on the dimerization equilibrium constant of $K_p = 2.6$ Torr (estimated by Osborne *et al*. in Ref. 37 of the main text) and the average partial pressure of AA-d_1 determined spectroscopically. This suggests that AA-d_1 clusters do not play a significant role in the observed photochemsitry. However, in our current configuration, the AA-d_1 concentration is potentially inhomogeneous in the photolyzed volume, and is significantly higher as the precursor gas flow expands into the cell. We can exclude neither the possibility that some clusters are present in some regions of the cell, nor that there could a non-equilibrium concentrations of clusters

It is difficult to quantify potential H_2O contamination on the walls of the flow cell, including the excimer windows. As described above, care was taken to ensure the isotopic purity of the synthesized AA-d_1 sample. Clean and dry excimer windows were installed prior to photolysis experiments, and a series of dry nitrogen flow and vacuum pumping cycles were conducted

before AA-d_1 was introduced. We used research grade N_2 and CO_2, and AA-d_1 was bubbled through the flow cell under experimental conditions for several minutes prior to the acquisition of photolysis data. Although the flow cell was not baked out at high temperature prior to photolysis experiments, the flow/pump cycles and AA-d_1 purging is expected to significantly reduce hydrogen contamination on the wall of the flow cell to a minimum. These details regarding sample cell preparation are available earlier in the Supporting Information.

Experimentally, we always observed that D_2O formation dominates the absorption spectra at long times (>80 ms), while the HOD signal simultaneously decreases (see Figs. 4A and 4B). We concluded that HOD is being converted to D_2O, secondary chemistry is dominated by deuteration, thus indicating that H_2O concentration must be low, and that the system is well passivated for deuterium over hydrogen.

It is possible that the excimer radiation initiates photochemistry of acrylic acid deposited on the laser windows; AA* + AA reactions could give rise to the products observed. The excimer windows are located approximately 1.27 cm from the probe beam. Photoproducts would need to be ejected into the central probe axis (central 1.2 mm beam waist) within the first 25-50 μs. It is less likely that the H in HOD comes from OH groups on the window. Given the 90% isotopic composition of the AA-d_1 precursor and complete reaction of HOD to D_2O, we expect species adsorbed on the excimer windows to be heavily depleted in reactive hydrogen.

References:

(*S1*) Rothman, L. S.; Gordon, I. E.; Barbe, A.; Benner, D. C.; Bernath, P. F.; Birk, M.; Boudon, V.; Brown, L. R.; Campargue, A.; Champion, J. -P.; Chance, K.; Coudert, L. H.; Dana, V.; Devi, V. M.; Fally, S.; Flaud, J. -M.; Gamache, R. R.; Goldman, A.; Jacquemart, D.; Kleiner,

I.; Lacome, N.; Lafferty, W. J.; Mandin, J. -Y.; Massie, S. T.; Mikhailenko, S. N.; Miller, C. E.; Moazzen-Ahmadi, N.; Naumenko, O. V.; Nikitin, A. V.; Orphal, J.; Perevalov, V. I.; Perrin, A.; Predoi-Cross, A.; Rinsland, C. P.; Rotger, M.; Šimečková, M.; Smith, M. A. H.; Sung, K.; Tashkun, S. A.; Tennyson, J.; Toth, R. A.; Vandaele, A. C.; Vander Auwera, J. The *HITRAN* 2008 Molecular Spectroscopic Database, *J. Quant. Spectrosc. Radiat. Transf.* **2009**, *110*, 533-572.

(*S2*) Toth, R. A.; HDO and D_2O Low Pressure, Long Path Spectra in the 600-3100 cm^{-1} Region. *J. Mol. Spectrosc*. **1999**, *195*, 73-97.

(*S3*) PGOPHER, a Program for Simulating Rotational Structure, C. M. Western, University of Bristol, http://pgopher.chm.bris.ac.uk.

(*S4*) Baldacci, A.; Ghersetti, S.; Hurlock, S. C.; Rao, K. N. Infrared Bands of $^{12}C_2HD$. *J. Mol. Spectrosc*. **1976**, *59*, 116-125.

(*S5*) CFOUR, a quantum chemical program package written by Stanton, J. F.; Gauss, J.; Harding, M. E.; Szalay P. G.; with contributions from Auer, A. A.; Bartlett, R. J.; Benedikt, U.; Berger, C.; Bernholdt, D. E.; Bomble, Y. J.; Christiansen, O.; Heckert, M.; Heun, O.; Huber, C.; Jagau, T. -C.; Jonsson, D.; Jusélius, J.; Klein, K.; Lauderdale, W. J.; Matthews, D. A.; Metzroth, T.; O'Neill, D. P.; Price, D. R.; Prochnow, E.; Ruud, K.; Schiffmann, F.; Stopkowicz, S.; Tajti, A.; Vázquez, J.; Wang, F.; Watts, J. D. and the integral packages MOLECULE (Almlöf J.; Taylor, P.R.), PROPS (Taylor, P. R.), ABACUS (Helgaker, T.; Aa. Jensen, H. J.; Jørgensen, P.; Olsen, J.), and ECP routines by Mitin, A. V.; van Wüllen, C. For the current version, see http://www.cfour.de.

(*S6*) Abrams, M. C.; Davis, S. P.; Rao, M. L. P.; Engleman, Jr., R. High-Resolution Fourier Transform Spectroscopy of the Vibration-Rotation Spectrum of the OD Radical. *J. Mol. Spectrosc*. **1994**, *165*, 57-74.

(*S7*) The acrylic acid spectrum was recorded at Pacific Northwest National Lab (PNNL) on March 19, 2010 and accessed from the PNNL database by Adam J. Fleisher at JILA on April 20, 2013. The original database reference is: Sharpe, S. W.; Johnson, T. J.; Sams, R. L.; Chu, P. M.; Rhoderick, G. C.; Johnson, P. A. Gas-Phase Databases for Quantitative Infrared Spectroscopy. *Appl. Spectrosc*. **2004**, *58*, 1452-146.

(*S8*) Gaussian 09, Revision B.01, Frisch, M. J.; Trucks, G. W.; Schlegel, H. B.; Scuseria, G. E.; Robb, M. A.; Cheeseman, J. R.; Scalmani, G.; Barone, V.; Mennucci, B.; Petersson, G. A.; Nakatsuji, H.; Caricato, M.; Li, X.; Hratchian, H. P.; Izmaylov, A. F.; Bloino, J.; Zheng, G.; Sonnenberg, J. L.; Hada, M.; Ehara, M.; Toyota, K.; Fukuda, R.; Hasegawa, J.; Ishida, M.; Nakajima, T.; Honda, Y.; Kitao, O.; Nakai, H.; Vreven, T.; Montgomery, J. A., Jr.; Peralta, J. E.; Ogliaro, F.; Bearpark, M.; Heyd, J. J.; Brothers, E.; Kudin, K. N.; Staroverov, V. N.; Kobayashi, R.; Normand, J.; Raghavachari, K.; Rendell, A.; Burant, J. C.; Iyengar, S. S.; Tomasi, J.; Cossi, M.; Rega, N.; Millam, N. J.; Klene, M.; Knox, J. E.; Cross, J. B.; Bakken, V.; Adamo, C.; Jaramillo, J.; Gomperts, R.; Stratmann, R. E.; Yazyev, O.; Austin, A. J.; Cammi, R.; Pomelli, C.; Ochterski, J. W.; Martin, R. L.; Morokuma, K.; Zakrzewski, V. G.; Voth, G. A.; Salvador, P.; Dannenberg, J. J.; Dapprich, S.; Daniels, A. D.; Farkas, Ö.; Foresman, J. B.; Ortiz, J. V.; Cioslowski, J.; Fox, D. J. Gaussian, Inc., Wallingford CT, 2009.

(*S9*) Certain commercial equipment, instruments, or materials are identified in this paper in order to specify the experimental procedure adequately. Such identification is not intended to imply recommendation or endorsement by the National Institute of Standards and Technology,

nor is it intended to imply that the materials or equipment identified are necessarily the best available for the purpose.

(*S10*) Morita, H.; Fuke, K.; Nagakura, S. Electronic Structure and Spectra of Acrylic Acid in the Vapor and Condensed Phases. *Bull. Chem. Soc. Jpn.* **1976**, *49*, 922-928. In Figure 1 of the online edition of this article, the *y*-axis is missing decimal points which appear in the original paper copy. The reported gas phase molar absorptivity of acrylic acid at 193 nm (51.8×10^{3} cm^{-1}) is $\approx4.5\times10^{3}$ dm^{3} mol^{-1} cm^{-1}, which yields $\sigma_{AA} \approx 7.5\times10^{-18}$ cm^{2}.